

Analysis of the extent of interphase precipitation in V-HSLA steels through in-situ characterization of the γ/α transformation

Clark, S, Janik, V, Rijkenberg, A & Sridhar, S

Author post-print (accepted) deposited by Coventry University's Repository

Original citation & hyperlink:

Clark, S, Janik, V, Rijkenberg, A & Sridhar, S 2016, 'Analysis of the extent of interphase precipitation in V-HSLA steels through in-situ characterization of the γ/α transformation' *Materials Characterization*, vol 115, pp. 83-89

<https://dx.doi.org/10.1016/j.matchar.2016.03.021>

DOI 10.1016/j.matchar.2016.03.021

ISSN 1044-5803

ESSN 1873-4189

Publisher: Elsevier

NOTICE: this is the author's version of a work that was accepted for publication in *Materials Characterization*. Changes resulting from the publishing process, such as peer review, editing, corrections, structural formatting, and other quality control mechanisms may not be reflected in this document. Changes may have been made to this work since it was submitted for publication. A definitive version was subsequently published in *Materials Characterization*, [115, (2016)] DOI: 10.1016/j.matchar.2016.03.021

© 2016, Elsevier. Licensed under the Creative Commons Attribution-NonCommercial-NoDerivatives 4.0 International

<http://creativecommons.org/licenses/by-nc-nd/4.0/>

Copyright © and Moral Rights are retained by the author(s) and/ or other copyright owners. A copy can be downloaded for personal non-commercial research or study, without prior permission or charge. This item cannot be reproduced or quoted extensively from without first obtaining permission in writing from the copyright holder(s). The content must not be changed in any way or sold commercially in any format or medium without the formal permission of the copyright holders.

This document is the author's post-print version, incorporating any revisions agreed during the peer-review process. Some differences between the published version and this version may remain and you are advised to consult the published version if you wish to cite from it.

Analysis of the extent of interphase precipitation in V-HSLA steels through *in-situ* characterization of the γ/α transformation

Authors

Samuel Clark¹, Vit Janik¹, Arjan Rijkenberg², Seetharaman Sridhar¹

¹WMG, University of Warwick, Coventry, CV4 7AL, United Kingdom

²Tata Steel, 1970 CA IJmuiden, The Netherlands

Author Email Addresses:

Samuel Clark: S.J.Clark@warwick.ac.uk

Vit Janik: V.Janik@warwick.ac.uk

Arjan Rijkenberg: arjan.rijkenberg@tatasteel.com

Seetharaman Sridhar: S.Seetharaman@warwick.ac.uk

Corresponding Author Samuel Clark

Highlights

- *In-situ* characterization of γ/α transformation
- EBSD characterization of γ/α transformation orientation relationship
- Extent of interphase precipitation can be controlled through controlled cooling

Keywords

In-situ-EBSD, *In-Situ*-HT-CLSM, Interphase Precipitation, Orientation Relationships.

Abstract

In-situ characterization techniques have been applied to elucidate the influence of γ/α transformation upon the extent of interphase precipitation in a low-carbon, vanadium-HSLA steel. Electron Back-scattered diffraction analyses of the γ/α orientation relationship with continuous cooling at 2 and 10 K/s suggest that the proportion of ferrite likely to hold interphase precipitation varies little with cooling rate. However, TEM analyses show that the interphase precipitation refines with increasing cooling rate in this cooling range. With cooling rates in excess of 20 K/s, interphase precipitation is increasingly suppressed due to the increasingly diffusional-displacive nature of the Widmanstätten γ/α transformation that is activated. The present study illustrates that the extent and dimensions of interphase precipitation can be controlled through controlled cooling.

1) Introduction

The development of new hot-rolled high-strength formable steels offering innovative light-weight solutions to reduce vehicle weight is crucial for automotive designers to improve fuel economy without compromising safety, performance or manufacturability. This focus extends to the chassis system, where hot-rolled Advanced High Strength Steels (AHSS) with increased strength and improved stretch-flange formability over conventional High Strength Low Alloy (HSLA) steels are increasingly used. However, the advent of ever more demanding light-weight chassis designs requires that any intrinsic loss in stiffness due to down-gauging with higher strength steels is compensated with increased structural stiffness derived from geometrical optimization [1]. This challenge requires hot-rolled high-strength steels offering an unsurpassed freedom in design derived from a balance between stretchability and stretch-flange formability that is superior to that of AHSS used nowadays for chassis

applications [2]. The steel industry has responded to this challenge by developing nano-precipitation strengthened, single-phase ferritic steels based on various micro-alloying systems, including Ti or V based alloys [3–5]. These steels combine high stretchability and high stretch-flange formability due to single-phase ductile ferrite matrix in combination with high tensile strength derived from nano-precipitation hardening [6,7]. Apart from strengthening the matrix, this nano-precipitation hardening is beneficial to consume all carbon and to suppress the presence of cementite, which can impair stretch-flange formability [8].

In this context, interphase precipitation has recently re-gained substantial interest as its optimized exploitation leading to densely packed ordered arrays of precipitates contributes significantly to matrix strengthening through the Orowan mechanism [9]. Interphase precipitation can both occur on semi-coherent and incoherent γ/α interfaces [10–13] and its morphology can be both planar and curved [14], depending on the curved or faceted nature of the migrating incoherent interphase boundaries [15].

Okamoto [16] suggested that interphase precipitation in Niobium microalloyed steels was not associated with the $\{1\ 1\ 0\}\alpha$, rather that interphase precipitation could be found to be associated with many varying interfaces and can have different orientations within one single ferrite grain. Yen [17] found through the use of careful TEM analysis of isothermally transformed Ti-Mo low carbon steel that the sheet planes of interphase-precipitated carbides are oriented close to any one of the $(2\ 1\ 1)\ \alpha$, $(1\ 1\ 1)\ \alpha$, and $(2\ 1\ 0)\ \alpha$ planes rather than that of the commonly asserted $\{1\ 1\ 0\}\alpha$. A corollary of this finding is that the interphase precipitation mechanism is connected with the development of incoherent γ/α interfaces. Furthermore, recently, Furuhashi and co-workers [10–13] have shown through

analysis of partially transformed samples and the reconstruction of the parent austenite (γ -martensite), that the number density of interphase precipitates initially increases rapidly as the orientation angle between parent γ/α deviates ($\Delta\theta$) increasingly from the ideal Kurdjumov-Sachs Orientation Relationship (KS-OR).

The number density of interphase precipitates then stabilizes with $\Delta\theta$ greater than 5° [12]. Apart from KS-OR, the Nishiyama-Wassermann Orientation Relationship (NW-OR) provides an additional rational low-energy γ/α OR with partially coherent boundaries hindering α growth [18].

In this paper, using a suite of advanced *in-situ* characterization techniques, we aim to elucidate the OR at the γ/α interphase and its influence upon interphase precipitation for a near stoichiometric V-based alloy. Specifically, we aim to validate these hypotheses:

- Interphase precipitation is promoted by ferrite growth with a greater degree of incoherency of the γ/α interphase (deviation from the semi-coherent KS- and NW-OR's).
- The extent of interphase precipitation is influenced by cooling rate and the morphology of the resulting γ/α formation.

2) Experimental

2.1) Chemistry and pre-treating of the as received steel

The experimental material was provided by Tata Steel in the form of forged blocks with the

following composition (wt.%): 0.046 C, 1.60 Mn, 0.18 Si, 0.45 Al, 0.2 V, 0.005 N. Samples for thermal treatment and simultaneous characterization using *in-situ* EBSD were sectioned from the forged blocks, producing 6 x 32 mm sized strips with 250 μm thickness from which 3 mm diameter discs were punched using a Gatan Model 623 . The samples were subsequently thinned to 120 μm using a Buhler MiniMet 1000 Polisher Grinder with Precision Thinning Attachment on a 15 μm diamond-grinding disk. Further polishing was achieved using reinforced tape on a 2500 grit paper and final near-mirror polishing using a 1 μm diamond polishing compound.

The steel samples were heat-treated using a High-Temperature Confocal Laser Scanning Microscope (HT-CLSM), Yonekura MFG, VL2000DX-SVF17SP, with a super-pure Ar atmosphere achieved using an Agilent indicating O₂ trap in order to prevent excessive oxidation. The samples were heated at a rate of 5 K/s to 1473 K and held for 120 s in order to dissolve any V(C,N) precipitates in the as-received material. The samples were then rapidly quenched at a cooling rate of 30 K/s to room temperature through rapid exchange of the Ar atmosphere with He.

2.2) *In-Situ* HT-CLSM heat treatment and characterization

The samples were further heat-treated and imaged *in-situ* using High-Temperature Confocal Laser Scanning Microscopy (HT-CLSM). The heat-treatments used in these experiments were as follows: heating at 5 K/s to 1173 K followed by an isothermal hold for 180 s then continuously cooled at rates of 2, 5, 10 and 20 K/s to room temperature. Stacks of HT-CLSM micrographs were collected at a rate of 15 frames per second using 25 times magnification. These stacks were subsequently analyzed, the characteristic transformation temperatures were determined using ImageJ digital image analysis software.

Additional, samples for micro-hardness analysis were prepared in the form of cuboids with dimensions 5 by 5 by 0.5 mm and mirror polished using standard metallographical techniques. The samples were heat treated using HT-CLSM adopting corresponding thermal cycles to those used for the 3 mm diameter discs. After the thermal treatment was finished the samples were etched using 2% Nital solution, revealing the ferritic grain boundaries and allowing micro-hardness measurements to be taken from the interior of 8 allotriomorphic and polygonal ferritic grains for each condition. The Vickers micro-hardness measurements were performed using a Buehler Tukon 1102 micro-hardness tester employing 10 g load for a dwell time of 10 s. Further Vickers hardness measurements were undertaken in order to characterize the bulk microstructure in the form of line scans of 20 indents evenly distributed diagonally across the surface of the sample using the same Tukon 1102 micro-hardness tester employing 500 g load for a dwell time of 10 s.

2.3) *In-situ* EBSD heat treatment and characterization

In-situ High-Temperature Electron Backscatter Diffraction (HT-EBSD) Analysis was performed using a Gatan Murano hot stage Model 525 to characterize both the austenitic grain structure at 1173 K after heating at 5 K/s as well as the ferritic grain structure after continuous cooling at 2 and 10 K/s to 873 K. This was undertaken inside the chamber of Secondary Electron Microscope Carl Zeiss Gemini, equipped with Electron Back Scattered Diffraction camera Nordlys EBSD by Oxford Instruments. Samples for HT-EBSD were taken directly from the HT-CLSM after undergoing the thermal cycle as described above with aim to dissolve all preexisting V(C,N) precipitates. No further re-polishing or etching of the post-CLSM samples was necessary since sufficient surface quality was maintained after the HT-CLSM, leading to an EBSD indexing quality above 95%. EBSD data sets were acquired using a

25 kV accelerating voltage, a 240 μm aperture size, and a 0.5 μm step size. Analyses of the EBSD data sets were done with HKL Chanel 5 post processing software, with the .ctf files exported for further analysis using the MTEX texture analysis toolbox, MTEX-4.0.23 <http://mtex-toolbox.github.io> , for MATLAB, R20014b.

2.4) *In-situ* EBSD data post-processing

Following continuous cooling from 1173 K to 873 K at 2K/s and 10 K/s the EBSD maps corresponding with the start (austenitic) and final (ferritic) temperatures were aligned using oxides or MnS inclusions visible in both mapped areas as small non-indexing regions common to both the austenitic and ferritic EBSD scans.

The aligned γ/α EBSD maps were further post-processed in order to spatially quantify the OR between parent γ and daughter α . Subsequently, spatial distribution of $\Delta\theta$ is calculated, which is the difference between the measured OR and that of the closest fitting KS- or NW-OR variant. $\Delta\theta$ was determined using the Rodrigues-Frank parameterization as shown in Equation 1; Rodrigues-Frank parameterization was chosen as it provides an intuitive way of evaluating misorientation [19], where, \hat{r} is an axis and θ is the rotation angle.

$$\rho = \hat{r} \tan\left(\frac{\theta}{2}\right) \quad \hat{r} = [r_1, r_2, r_3] \quad (1)$$

Each of the 24 variants of the KS-OR and the 12 variants of the NW-OR were expressed as Rodrigues-Frank vectors using the orientation transformation matrices described in References [20] and [21] respectively, and calculated according to the relations described in Reference [22].

For the entire population of γ grains within the sampled area of $120 \times 80 \mu\text{m}$, the

misorientation θ_{measured} between the mean orientation of each γ grain and the individual orientation of α -indexed pixels within its γ grain boundary was computed.

$$\Delta\theta = \min. |\theta_{OR\ i}^{\text{variant } j} - \theta_{\text{Measured}}| \quad (2)$$

Next, the $\Delta\theta$ between θ_{measured} and every variant of KS-OR and NW-OR was determined by calculating the minimum absolute difference between the two θ orientations. The closest matching OR, i , where, ($i=1=K-S$, $2=N-W$, and $3=$ None Detected), and OR variant, j , where, ($j=1:24$ for K-S and $1:12$ for N-W) for each α EBSD measurement was selected according to Equation 2. The fitting of an OR was deemed to be inappropriate if $\theta \leq 5^\circ$.

3) Results and Discussion

3.1) *In-situ* EBSD characterization of the low-energy OR's during γ/α transformation

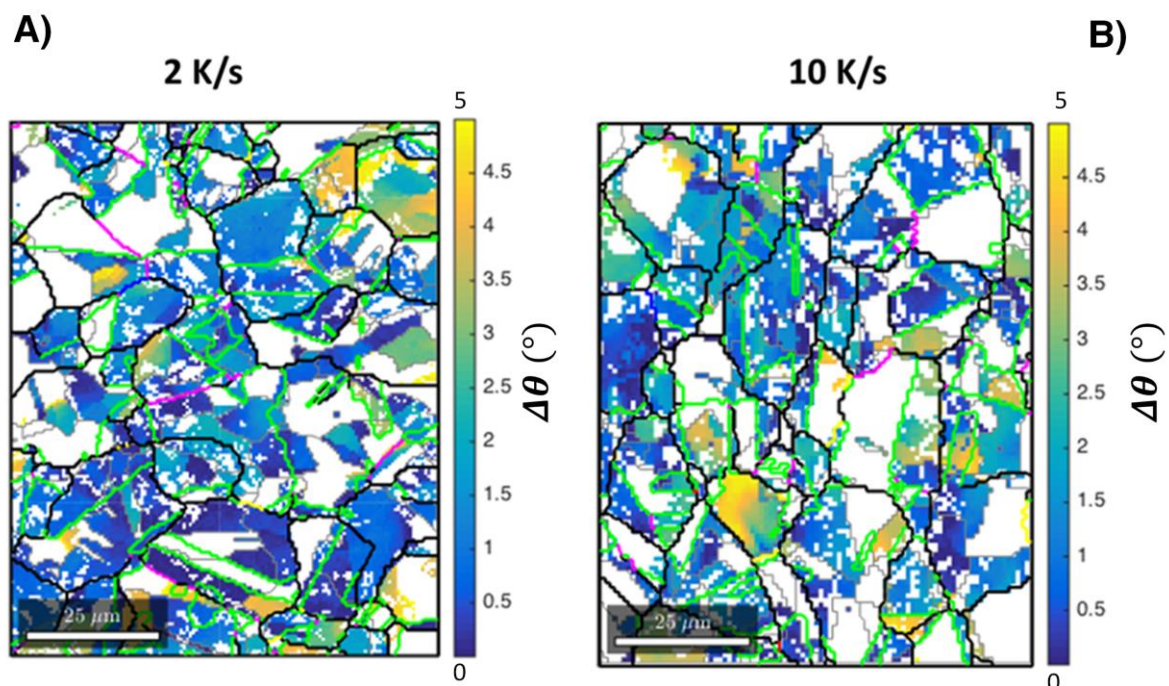


Figure 1A and 1B Overlapping EBSD micrographs of initial austenite and resulting ferritic microstructure acquired *in-situ* and processed with MTEX texture toolbox; cooling rates 2

K/s A), and 10K/s B). Color-coding for the austenitic grain boundaries: black = random grain boundaries, green = coincidence site lattice (CLS) boundaries Σ 3, blue = CLS Σ 5, red = CLS Σ 7, magenta = CLS Σ 9 and yellow = CLS Σ 11. Distribution of the Ferrite orientation exhibiting a minimum $\Delta\theta$ of less than 5° with regard to a low-energy orientation relationship with the original austenitic matrix.

Figure 1 shows for two different cooling rates (i.e., A, 2 and B, 10 K/s), the distribution and magnitude of $\Delta\theta$ mapped for regions where either the KS- or NW-OR were fitted for continuous cooling at 2 and 10 K/s, respectively.

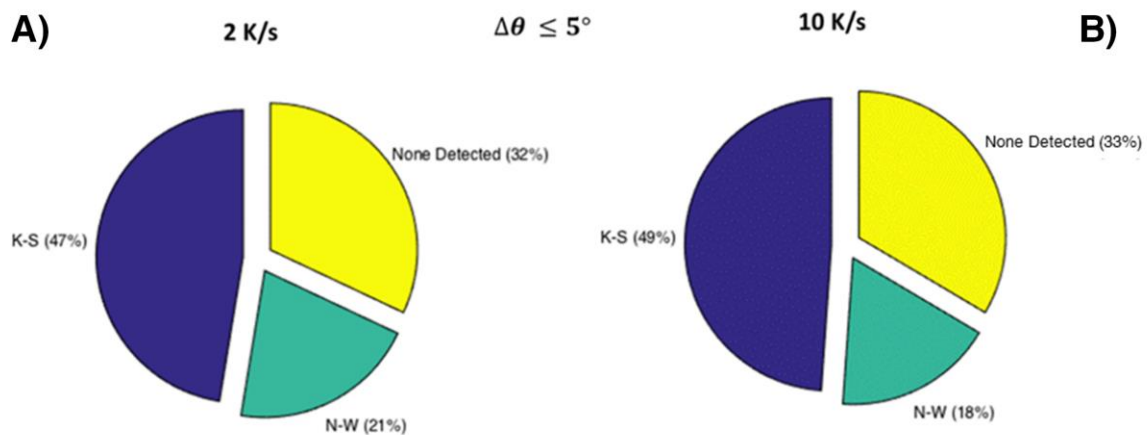


Figure 2A and B show the surface fraction of the Ferrite EBSD mapped region exhibiting a minimum $\Delta\theta$ below 5° with regard to γ/α low-energy K-S and N-W orientation relationships as well as the surface fraction with $\Delta\theta$ higher than 5° (labeled as “None Detected”) with the K-S and N-W orientation relationships.

Figure 2A and 2B show the surface area fractions for which the minimum $\Delta\theta$ is less than 5° with regard to the KS-OR, NW-OR, and regions where $\Delta\theta$ is larger than 5° and where no KS-OR or NW-OR was detected. A close match (i.e., $\Delta\theta < 5^\circ$) with the KS-OR was found for 47% and 49% of the mapped area at 2 and 10 K/s, respectively. For the NW-OR, this was

considerably lower, with fractions of 21% and 18% of the mapped area at 2 and 10 K/s, respectively. The remaining area has a $\Delta\theta$ value $\Delta\theta$ which is greater than 5° , showing no close fit with either the K-S or N-W orientation relationship.

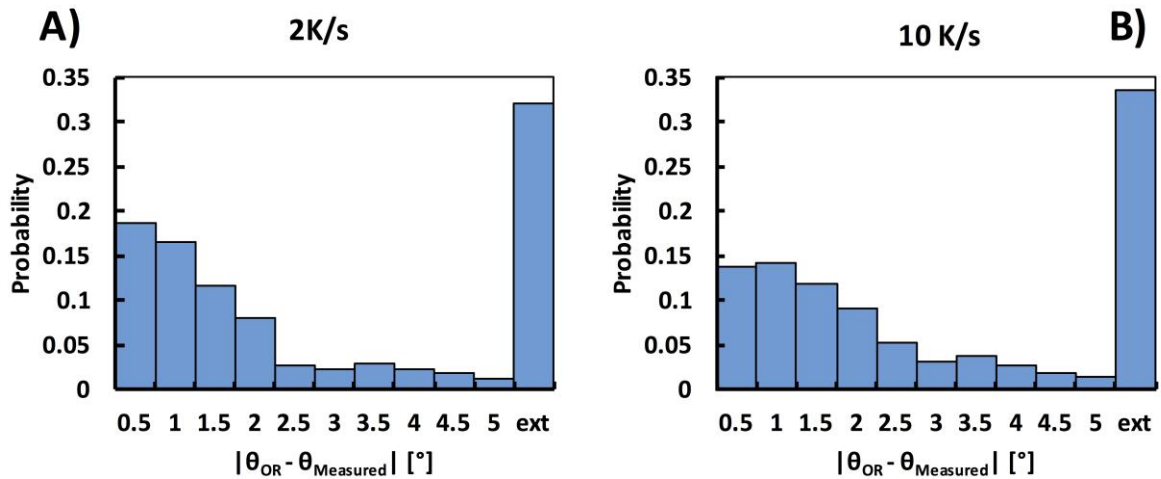


Figure 1 Distribution of the minimum $\Delta\theta$ values below 5° with regard to the K-S and N-W low-energy orientation relationships.

Figure 3A and 3B show the corresponding normalized probability histograms displaying the distribution of $\Delta\theta$, for $\Delta\theta$ values less than 5° after continuous cooling at 2 and 10 K/s respectively.

3.2) *In-situ* HT-CLSM characterization of γ/α transformation

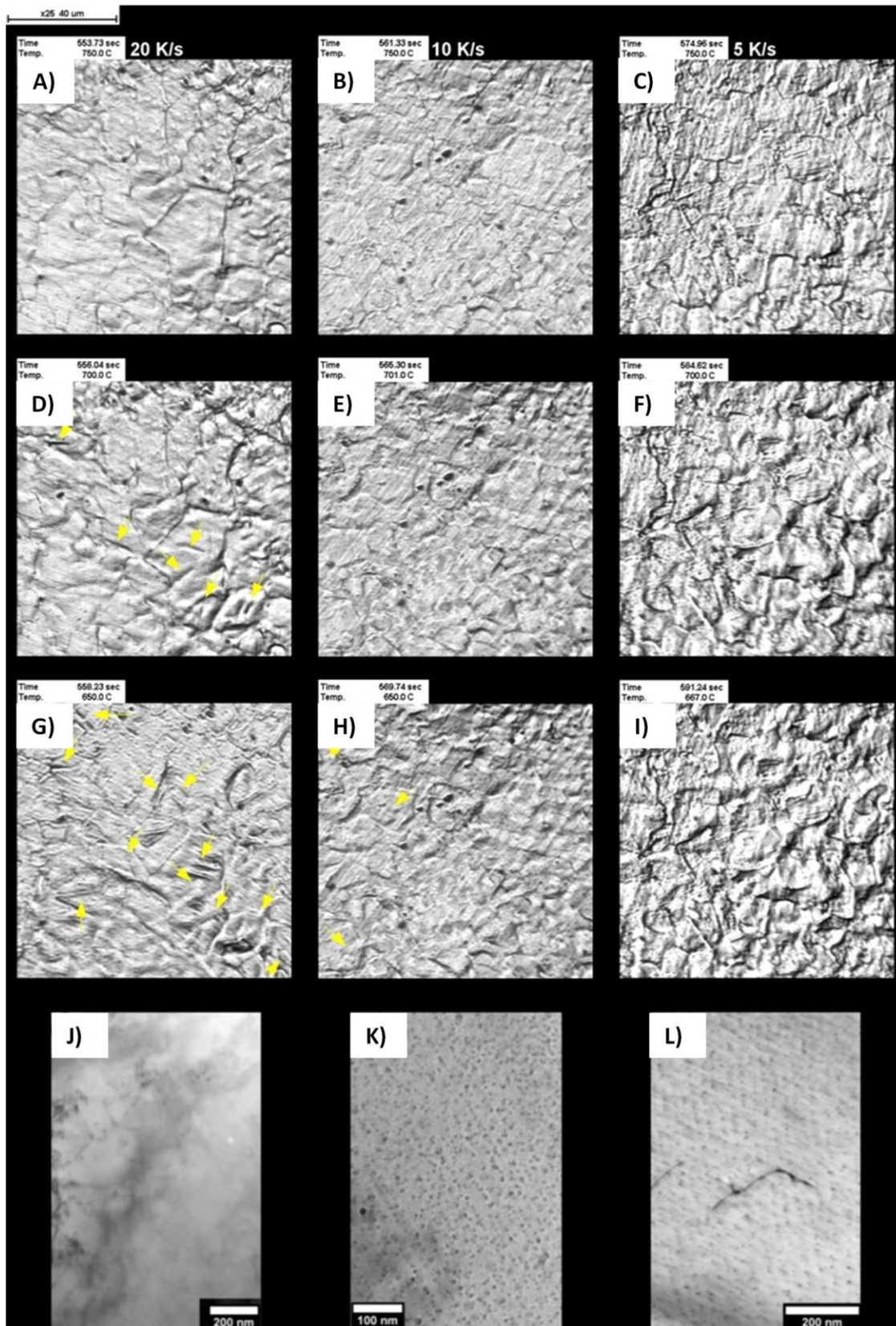


Figure 2 Montage of HT-CLSM micrographs and typical TEM micrographs of the precipitates observed within each foil after continuous cooling at 20, 10 and 5 K/s, respectively. Full transformation video included as supplementary material.

In order to further elucidate the transformation kinetics, samples were imaged using *in-situ* using HT-CLSM. These samples were first heat treated by reheating to 1473 K for full precipitate dissolution, followed by rapid cooling at 30 K/s to room temperature to refine the microstructure. Next, the samples were reheated to 1173 K and subjected to four different continuous cooling rates from the austenitic region to room temperature, i.e., 20, 10, 5, and 2 K/s. This allowed the assessment of the characteristic transformation start temperatures to be deduced through direct observation of the γ/α interface nature. Regions where Widmanstätten ferrite formation is observed during continuous cooling have been marked with yellow arrows in specific micrographs in Figure 4. The regions of Widmanstätten ferrite are distinguished by the rapid transformation kinetics and the 'jagged' interphase morphology, in contrast to that of the interphases of allotriomorphic ferrite.

Reheating the supersaturated ferritic matrix to 1173 K and continuously cooling at 20 K/s (Figure 4 A,D,G) led to pro-eutectoid allotriomorphic ferrite nucleating at 1032 K, followed by the nucleation of displacive ferrite, i.e., primarily Widmanstätten ferrite, at 768 K, marked with yellow arrows. With continuous cooling rates of 10 (Figure 4 B,E,H) and 5 K/s (Figure 4 C,F,I) austenite decomposes to almost purely pro-eutectoid allotriomorphic ferrite at a start temperature of 1035 and 1041 K, respectively, regions where Widmanstätten ferrite nucleates has once again been highlighted with yellow arrows.

Figures 4J to 4L show bright field TEM micrographs of regions where interphase precipitation is observed after continuous cooling from 1173 K at 20, 10 and 5 K/s, respectively, to room temperature. Four TEM samples were prepared for each condition. As

the mean ferritic grain size in each case was less than 15 μm there were many regions of clearly identifiable ferrite grains within the thin transparent rim of each TEM sample. The micrographs presented were typical of the many regions observed. The TEM micrographs show that the increasing cooling rate from 5 to 10 K/s refines interphase precipitation. However, a further increase of the cooling rate to 20 K/s results in a microstructure that is devoid of precipitates. The presence of random precipitates are not observed due to the insufficient time for such precipitates to nucleate.

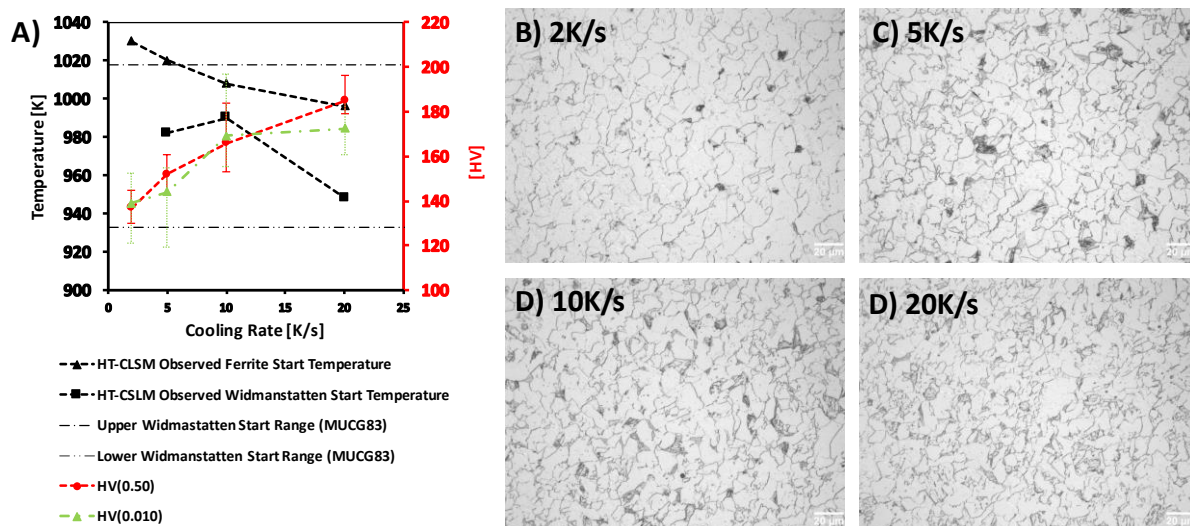


Figure 5 A shows the the measure allotriomorphic and Widmanstätten ferrite start temperatures for the bulk block samples plotted with the predicted Widmanstätten start temperature range predicted using the MAP program MUCG83, bulk HV(0.50) measurements and targeted HV(0.010) micro-hardness of the allotriomorphic regions. Figures 5 B-D show optical micrographs after continuous cooling from 1173 K at the marked cooling rates.

Figure 5 A shows the measured allotriomorphic and Widmanstätten ferrite start temperatures for the bulk 5 by 5 by 0.5 mm block samples plotted along with the predicted Widmanstätten start temperature range predicted using the MAP program MUCG83 [23]. It is shown that the experimentally observed start temperatures, determined through carefully analyzing the first regions to transform within the imaged surface area lie within

the range of start temperatures predicted by MUCG83 for this composition. In addition, Figure 5A shows the results bulk HV(0.50) measurements and targeted HV(0.010) micro-hardness of the allotriomorphic regions. Figures 5 B-D show the corresponding optical micrographs obtained after continuous cooling from 1173 K at the marked cooling rates. As 20 HV(0.50) measurements were made and the indents covered many grains incorporating both the allotriomorphic and Widmanstätten ferrite, it is shown that generally with increasing cooling rate the measured micro-hardness increases with the cooling rate. However, with the targeted use of HV(0.010) indents it was possible to generate indents which lay within the allotriomorphic or polygonal ferritic grains. Whilst the measured Vickers hardness increases with increasing cooling rate in general the Vickers hardness increases more profoundly between the cooling rates of 5 and 10 K/s. The Vickers hardness of the allotriomorphic regions in the 20 K/s condition appear to have plateaued and remain at a similar level to that which is measured in the 10 K/s condition. This step in hardness appears to correspond to the refinement of the interphase precipitation observed in Figure 4K and L at the same cooling rates.

However, as the targeted micro-hardness measurements plateau between the cooling rates of 10 K/s and 20 K/s whereas, no interphase precipitates are observed in Figure 4J. This suggests that other strengthening mechanisms may also be contributing to the measured hardness and becoming increasingly significant with increasing cooling rate such as, dislocation strengthening.

The kinetics of Widmanstätten ferrite have been investigated *in-situ* previously [24–26] and it has been shown that the free surface of a cross section has an influence upon the kinetics

of Widmanstätten ferrite growth. The average growth rate of Widmanstätten plates measured *in-situ* for free-surface samples is estimated to be one order of magnitude greater than that measured for the bulk. One explanation for this difference in average growth rate is that in case of a free surface the growth kinetics are close to para-equilibrium, whereas for the bulk local partitioning equilibrium is believed to be negligible [26]. Another aspect that may play a role is that the Widmanstätten ferrite start temperature is also influenced by the presence of a free surface. It has been found that for martensitic transformations the free surface allows martensitic transformations to occur at a higher temperature than in bulk material. The reason for this is the fact that a free surface compared to bulk facilitates the shape deformation, i.e., volume expansion, accompanying the transformation from austenite to martensite [27].

With greater cooling rates or lower transformation temperatures, the mobility of interfaces with a random orientation relationship with the parent austenite decreases, whereas the mobility of that of the coherent interface increases and becomes dominant [28]. The nucleation of Widmanstätten ferrite also becomes increasingly significant [29], in particular since the growth rate of Widmanstätten ferrite is much greater than that of spherical allotriomorphic ferrite [30]. In addition, the plate shape of Widmanstätten allows solutes to partition to the sides of the growing plate rather than pile up ahead of the plate as is the case with allotriomorphic ferrite [31]. In the case of Widmanstätten ferrite, it is conceivable that this partitioning of the solute to the side of growing plates prevents the formation of interphase precipitates.

Conventionally, it is thought that an allotriomorphic ferrite grain nucleates and grows at an austenite grain boundary with a coherent, low-energy OR with one of the surrounding

austenite grains. However, these allotriomorphic ferrite grains will have a different OR with the other neighboring austenite grain - or grains in case of a triple point. This means that an allotriomorphic ferrite grain will maintain a semi-coherent γ/α interphase with one parent austenite grain, and have one or two additional γ/α interphase boundaries which can either be semi-coherent or incoherent. In case of an incoherent γ/α interphase boundary, this can either lead to a interphase that is smoothly curved or has a faceted nature with various length scales [15]. Therefore, a significant amount of curved or planar arrays of interphase precipitation can be expected for the incoherent side of the allotriomorphic ferrite grain, whereas its coherent side where a low energy OR is maintained will show no interphase precipitation.

For the semi-coherent faceted side of an allotriomorph where a low energy OR is obeyed, it is not fully understood why no interphase precipitation is present. It has been suggested that the γ/α interface with a non-K-S OR has a higher interfacial energy than that of a K-S OR γ/α interface and hence that a non-K-S interface requires less energy for the formation of a critical nucleus. Additionally, solute atoms are known to segregate more readily to incoherent interfaces as the diffusivity of solutes at incoherent interfaces is higher [12], increasing the driving force for interphase precipitation. Furthermore, it is unlikely that an allotriomorphic ferrite grain will exhibit dual orientation that will accommodate a low energy OR across the austenite grain boundary or grain boundaries in case of a triple point [18]. As a consequence, it is unlikely that interphase precipitation can be completely eliminated in case of allotriomorphic ferrite nucleation.

In contrast, Widmanstätten ferrite will only nucleate and grow from the side of the austenite grain boundary exhibiting a low-energy OR as an invariant line between austenite

and ferrite cannot be sustained with large values of $\Delta\theta$ [32]. Therefore, as $\Delta\theta$ is always low, interphase precipitation is never expected to occur in Widmanstätten ferrite as the aforementioned factors favoring interphase precipitation for incoherent interfaces in case of allotriomorphic ferrite are not valid for the nucleation and growth of Widmanstätten ferrite.

It has been shown that in the case of precipitates, nucleating on incoherent inclusions in the matrix, do not hold any specific orientation relationship with that matrix [33]. As such, idiomorphic ferrite, which nucleates inside austenite grains and has a tendency to nucleate on non-metallic inclusions, is likely to have an orientation which substantially deviates from KS-OR. Hence, it is also expected that idiomorphic ferrite may exhibit interphase precipitation. Based on this, it is conceivable that the amount of interphase precipitation can be significantly enhanced through the optimization of incoherent particles in the steel matrix for effective nucleation of idiomorphic ferrite within austenite grains. Additional high resolution TEM study coupled with dilatometric experiments and in-situ HT-CLSM is currently under way to provide detailed information on precipitation morphology and will be published separately.

4) Summary

In the present work, using *in-situ* characterization techniques, the influence of γ/α transformation upon the extent of interphase precipitation in a low-carbon vanadium-HSLA steel was investigated. EBSD analyses of the γ/α OR of samples subjected to continuous cooling of 2 and 10 K/s suggest that the proportion of ferrite likely to hold interphase precipitation varies little with cooling rate. In the present study, EBSD indicates that circa 32% and 34% of the ferrite microstructure will exhibit interphase precipitation with

continuous cooling at 2 and 10 K/s, respectively, to room temperature. However, *a posteriori* TEM characterization does show that an increase in cooling rate from 5 to 10 K/s is coupled with a refinement of interphase precipitation in terms of carbide row spacing. At higher cooling rates, i.e., in excess of 20 K/s, interphase precipitation is increasingly suppressed due to the increasingly diffusional-displacive nature of the Widmanstätten γ/α transformation that is activated. It is suggested that interphase precipitation is not possible in Widmanstätten ferrite due to the lack of solute 'pile-up' ahead of the advancing γ/α interface. As a result, the critical concentration of solute at the interface required for carbide precipitation is not reached. This in turn implies that the extent and dimensions of interphase precipitation can be controlled through a controlled cooling.

Acknowledgements

Authors are thankful to Tata Steel for providing the experimental material. Financial support from the EPSRC grant EP/L018632/1 "Micro-structuring micro-alloyed steels via non-metallic precipitate formation" and financial assistance from the WMG Centre High Value Manufacturing Catapult are gratefully acknowledged.

References

- [1] C.M. Sonsino, Light-weight design chances using high-strength steels, *Materwiss. Werksttech.* 38 (2007) 9–22.
- [2] A. Rijkenberg, A. Blowey, P. Bellina, C. Wooffindin, Advanced High Stretch-Flange Formability Steels for Chassis & Suspension Applications 3 . Product concept : tensile properties and microstructure, in: 4th Int. Conf. Steels Cars Truck. SCT2014, Braunschweig, 2014: pp. 426–433.

- [3] T. Gladman, *The Physical Metallurgy of Microalloyed Steels*, Institute of Materials, 2002.
- [4] T. Baker, Processes, microstructure and properties of vanadium microalloyed steels, *Mater. Sci. Technol.* 25 (2009) 1083–1107.
- [5] R. Lagneborg, B. Hutchinson, T. Siwecki, S. Zajac, *The Role of Vanadium in Microalloyed Steels*, 2nd ed., Swerea KIMAB, Stockholm, 2014.
- [6] Y. Funakawa, T. Shiozaki, K. Tomita, T. Saito, H. Nakata, M. Suwa, et al., High Tensile Hot Rolled Steel Sheet And Method For Production Therof, 01980929.2, 2002.
- [7] R.A. Rijkenberg, A high-strength hot-rolled steel strip or sheet with excellent formability and fatigue performance and a method of manufacturing said steel strip or sheet, WO2014EP52334 20140206, 2014.
- [8] Y. Funakawa, T. Shiozaki, K. Tomita, T. Yamamoto, E. Maeda, Development of High Strength Hot-rolled Sheet Steel Consisting of Ferrite and Nanometer-sized Carbides, *ISIJ Int.* 44 (2004) 1945–1951.
- [9] M.-Y. Chen, M. Gouné, M. Verdier, Y. Bréchet, J.-R. Yang, Interphase precipitation in vanadium-alloyed steels: Strengthening contribution and morphological variability with austenite to ferrite transformation, *Acta Mater.* 64 (2014) 78–92.
- [10] T. Murakami, H. Hatano, G. Miyamoto, T. Furuhashi, Effects of Ferrite Growth Rate on Interphase Boundary Precipitation in V Microalloyed Steels, *ISIJ Int.* 52 (2012) 616–625.
- [11] G. Miyamoto, R. Hori, B. Poorganji, T. Furuhashi, Crystallographic analysis of proeutectoid ferrite/austenite interface and interphase precipitation of vanadium

- carbide in medium-carbon steel, *Metall. Mater. Trans. A Phys. Metall. Mater. Sci.* 44 (2013) 3436–3443.
- [12] Y.-J. Zhang, G. Miyamoto, K. Shinbo, T. Furuhashi, Effects of α/γ orientation relationship on VC interphase precipitation in low-carbon steels, *Scr. Mater.* 69 (2013) 17–20.
- [13] Y. Zhang, G. Miyamoto, K. Shinbo, T. Furuhashi, T. Ohmura, T. Suzuki, et al., Effects of transformation temperature on VC interphase precipitation and resultant hardness in low-carbon steels, *Acta Mater.* 84 (2015) 375–384.
- [14] R.A. Ricks, P.R. Howell, The formation of discrete precipitate dispersions on mobile interphase boundaries in iron-base alloys, *Acta Metall.* 31 (1983) 853–861.
- [15] T.B. Massalski, D.E. Laughlin, W. a. Soffa, The nature and role of incoherent interphase interfaces in diffusional solid-solid phase transformations, *Metall. Mater. Trans. A.* 37 (2006) 825–831.
- [16] R. Okamoto, a. Borgenstam, J. Ågren, Interphase precipitation in niobium-microalloyed steels, *Acta Mater.* 58 (2010) 4783–4790.
- [17] H.-W. Yen, P.-Y. Chen, C.-Y. Huang, J.-R. Yang, Interphase precipitation of nanometer-sized carbides in a titanium–molybdenum-bearing low-carbon steel, *Acta Mater.* 59 (2011) 6264–6274.
- [18] J.M. Howe, H.I. Aaronson, J.P. Hirth, Aspects of interphase boundary structure in diffusional phase transformations, *Acta Mater.* 48 (2000) 3977–3984.
- [19] K. Verbeken, L. Barbé, D. Raabe, Evaluation of the Crystallographic Orientation Relationships between FCC and BCC Phases in TRIP Steels, *ISIJ Int.* 49 (2009)

- 1601–1609.
- [20] H. Kitahara, R. Ueji, N. Tsuji, Y. Minamino, Crystallographic features of lath martensite in low-carbon steel, *Acta Mater.* 54 (2006) 1279–1288.
- [21] H. Kitahara, R. Ueji, M. Ueda, N. Tsuji, Y. Minamino, Crystallographic analysis of plate martensite in Fe-28.5 at.% Ni by FE-SEM/EBSD, *Mater. Charact.* 54 (2005) 378–386.
- [22] A. Morawiec, *Orientations and Rotations*, Springer Berlin Heidelberg, Berlin, 2004.
- [23] M. Peet, H.K.D.H. Bhadeshia, Program MAP_STEEL_MUCG83, *Mater. Algorithms Proj. Progr. Libr.* (2006).
- [24] D. Phelan, R. Dippenaar, Widmanstätten ferrite plate formation in low-carbon steels, *Metall. Mater. Trans. A.* 35 (2004) 3701–3706.
- [25] D. Phelan, N. Stanford, R. Dippenaar, In situ observations of Widmanstätten ferrite formation in a low-carbon steel, *Mater. Sci. Eng. A.* 407 (2005) 127–134.
- [26] X.L. Wan, R. Wei, L. Cheng, M. Enomoto, Y. Adachi, Lengthening kinetics of ferrite plates in high-strength low-carbon low alloy steel, *J. Mater. Sci.* 48 (2013) 4345–4355.
- [27] J. Pak, D. Suh, H. Bhadeshia, Displacive Phase Transformation and Surface Effects Associated with Confocal Laser Scanning Microscopy, *Metall. Mater. Trans. A.* 43 (2012) 4520–4525.
- [28] H.K.D.H. Bhadeshia, R.W.K. Honeycombe, *Steels Microstructure and Properties*, Third Edit, Butterworth-Heinemann, Oxford, 2006.
- [29] R.L. Bodnar, S.S. Hansen, Effects of austenite grain size and cooling rate on

- Widmanst?ttten ferrite formation in low-alloy steels, *Metall. Mater. Trans. A.* 25 (1994) 665–675.
- [30] M. Enomoto, T. Sonoyama, H. Yada, Kinetics of austenite to ferrite transformation in 3 mass% Mn low carbon steels, *Mater. Trans. JIM.* 39 (1998) 189–195.
- [31] H.K.D.H. Bhadeshia, Phase transformations contributing to the properties of modern steels, *Bull. Polish Acad. Sci. Tech. Sci.* 58 (2010) 255–265.
- [32] D.W. Kim, R.S. Qin, H.K.D.H. Bhadeshia, Transformation texture of allotriomorphic ferrite in steel, *Mater. Sci. Technol.* 25 (2009) 892–895.
- [33] T. Furuhashi, T. Maki, Variant selection in heterogeneous nucleation on defects in diffusional phase transformation and precipitation, *Mater. Sci. Eng. A.* 312 (2001) 145–154.